RSC Advances

PAPER

View Article Online
View Journal | View Issue

Open Access Article. Published on 08 December 2021. Downloaded on 2/7/2026 7:15:34 PM.
This article is licensed under a Creative Commons Attribution-NonCommercial 3.0 Unported Licence.

Check for updates

Cite this: *RSC Adv.*, 2021, **11**, 39153

Electroless deposition of Ni–P/Au coating on Cu substrate with improved corrosion resistance from Au(III)–DMH based cyanide-free plating bath using hypophosphite as a reducing agent†

Bo Wu,[a] Baizhao Tan,[a] Guizhen Tan,[a] Ming Zeng,[a] Jinyi Luo,[a] Guanghui Hu,[a] Jiye Luo,[a] Zhifeng Hao,*[a] Shaomei Lai[b] and Binyun Liu*[b]

The green cyanide-free gold deposition is an important development direction in electroless gold plating. However, the commonly Au(I) based cyanide-free gold plating bath always suffers from severe corrosion to the Ni–P layer and unsatisfactory service life of the bath. In this work, a green and environmentally friendly cyanide-free gold plating bath was developed with hypophosphite added as a reducing agent into the Au(III)–DMH (5,5-dimethylhydantoin) based plating bath to retard the corrosion of the Ni–P layer. SEM micrographs combined with XRD and XPS analysis indicated that the electroless deposited gold was pure and compact. And XRD also revealed that the oriented deposition of gold was growing preferentially on Au (111). Corrosion tests, including salt spray tests, potentiodynamic polarization tests, and electrochemical impedance spectroscopy tests, indicated that the obtained Cu/Ni–P/Au coatings had significantly improved corrosion resistance performance with the loading of hypophosphite as the reducing agent. The baths remained transparent and no turbidity or precipitates were detected for 210 days, reflecting good stability. The detection for the Ni^{2+} concentration in the bath showed that adding hypophosphite could retard the replacement reaction between Au^{3+} and the Ni–P layer in part and this is important for decreasing the severe corrosion of the Ni–P layer. Moreover, Au was inactive for catalyzing the oxidation of hypophosphite during the deposition process which was confirmed furthermore *via* quantum chemical calculations. Therefore, our developed green cyanide-free electroless gold deposition process can beneficially provide research value and application prospects in microelectronic industry.

Received 29th October 2021
Accepted 1st December 2021

DOI: 10.1039/d1ra07952b

rsc.li/rsc-advances

1. Introduction

Copper is popular in the electronic field because of its high conductivity and low price. However, copper has poor oxidation and corrosion resistance. Oxidation and corrosion products will hinder the conduction of electronic circuits, so it is necessary to carry out surface protection treatments on copper. Gold has excellent electrical function and chemical stability, and can provide an ideal corrosion protection effect on copper.[1] It is not recommended to deposit gold directly on copper, because copper will diffuse to the gold layer under the high temperature of wire bonding and encapsulation processes.[2] A nickel–phosphorus alloy can be used as a barrier to prevent diffusion.[3,4] In electronics, it is a common surface treatment to deposit nickel–phosphorus alloy and gold on the copper substrate in turn. It is usually realized through the electroless nickel/immersion gold (ENIG) process. The Cu/Ni–P/Au multi-layer film has excellent corrosion resistance and oxidation resistance compared with bare copper. The Au layer is thin soft pure gold except for electrical contact materials, and the thickness is usually about 0.03–0.1 μm. Although gold is an inert metal, it may be porous, especially at low thickness.[5] These pores induce the corrosion of the sublayer. The porosity of the gold layer obtained through immersion process had been reported as a fatal shortcoming.[6] Therefore, the deposition of a dense Au layer is very important to improve the corrosion resistance of Cu/Ni–P/Au multi-layer film.

In the traditional gold deposition, CN^- is widely used as a good complexing agent for Au^+ to form $Au(CN)_2^-$ coordination ion with high stability constant (K_f) of 10^{38}, which avoids the disproportionation reaction generally and retards bath decomposition effectively.[7] However, the complexing agent of cyanide in baths is highly toxic, and CN^- is also in poor compatibility with photoresists, which is harmful to the performance of

[a]Guangdong Provincial Key Laboratory of Plant Resources Biorefinery, School of Chemical Engineering and Light Industry, Guangdong University of Technology, Guangzhou 510006, China. E-mail: haozf@gdut.edu.cn

[b]Guangdong Toneset Science & Technology Co., Ltd, Guangzhou 511400, China. E-mail: beston@ghtech.com

† Electronic supplementary information (ESI) available. See DOI: 10.1039/d1ra07952b

© 2021 The Author(s). Published by the Royal Society of Chemistry

Open Access Article. Published on 08 December 2021. Downloaded on 2/7/2026 7:15:34 PM.
This article is licensed under a Creative Commons Attribution-NonCommercial 3.0 Unported Licence.

electronic products. With the improvement of environmental consciousness and for the manufacture of high-reliability precision electronic equipment, significant efforts have been made to find alternatives of CN^-. In the Au(I) based cyanide-free electroless plating baths, sulfite bath ($K_f[Au(SO_3)_2{}^{3-}] = 10^{26.8}$) and thiosulfate bath ($K_f[Au(S_2O_3)_2{}^{3-}] = 10^{26.1}$) were widely studied.[1,8] Unfortunately, the optimized operating conditions of pH for both baths were above 8.[9–11] In a high-temperature and alkaline environment (pH > 8), the photoresist will dissolve and its organic products will contaminate the bath. Accordingly, Kato *et al.*[12] and Osaka *et al.*[13] proposed a nearly neutral gold plating bath containing both sulfite and thiosulfate as mixed complexing agents ($K_f[Au(S_2O_3)(SO_3)^{3-}] = 10^{27.1}$).[14] However, this neutral gold plating bath suffered from the co-deposition of S element.[15] The presence of S atom will reduce the weldability and corrosion resistance of coatings.[16,17] Moreover, this type of bath was not stable sufficiently in whole service life. Recently, mercaptosuccinic acid and L-cysteine have been used as cyanide-free ligands for Au^+.[18,19] The sulfhydryl group has a very strong coordination ability, and can even replace part of CN^- in $Au(CN)_2{}^-$.[20] However, the smell of mercaptosuccinic acid and L-cysteine are unpleasant, especially under high-temperature reaction conditions. It remains challenging to develop green and environmental friendly cyanide-free Au(I) based plating baths.

In aqueous solution, Au^{3+} is more stable than Au^+, so it has been favored by more researchers in recent years. 5,5-Dimethylhydantoin (DMH),[21–24] theophylline,[25] and hypoxanthine[26,27] were cyanide-free complexing agents used in electroplating baths with Au^{3+} as the main salt. Among the three new complexing agents, DMH has been studied most. DMH is a nitrogen heterocyclic organic compound with low price, strong coordination ability, and good solubility in water. After the N atom between its two C=O bonds ionizes H^+, it can form DMH^- ion and then coordinate with Au^{3+} to form a four-coordinate complex.[22,28,29] The stability constant of $Au(DMH)_4{}^-$ which is square planar in geometry is 10^{21}.[1] The cyanide-free gold plating system with DMH as a complex can electrodeposit bright gold layer. As we all know, electroless plating is an essential way of metal deposition due to its unique advantages. Uniform thickness of coatings can be obtained *via* electroless plating, especially for parts or products with complex geometry. For the unconnected metal surface or non-conductive nonmetal surface, electroless plating is of competence, while electroplating is powerless.[30] Therefore, it is of great significance to study Au^{3+} in electroless plating systems and it is expected to solve the problem of instability of cyanide-free plating baths. However, other problems will follow. ENIG process relies on the replacement reaction of gold ions and nickel atoms to achieve gold deposition, and this process leads to the unavoidable corrosive behavior of gold ions to Ni–P layer. The black pad phenomenon,[31] also known as black nickel, which will reduce the corrosion resistance of the coating, will occur if the corrosion of gold ions is serious. According to eqn (1) and (2), it can be known that when depositing the same number of gold atoms, Au^{3+} consumes Ni atoms three times more than Au^+, which means that the Au^{3+} based gold plating bath is more prone to black pad. As reported by Wang *et al.*, although the Au(III)–ChCl based immersion gold plating bath was very stable, the black pad appeared and the coating could not effectively protect the copper substrate.[32] Thus, Au^{3+} is usually disliked in electroless process.

$$2Au^+ + Ni \rightarrow Ni^{2+} + 2Au \quad (1)$$

$$2Au^{3+} + 3Ni \rightarrow 3Ni^{2+} + 2Au \quad (2)$$

It may be an effective strategy to replace nickel atom with a reductant to provide electrons and participate in the reaction by adding reducing agents. Although this strategy has been reported in electroless gold plating, the reports mainly used $KAu(CN)_2$ as the gold salt and focused on the plating rate and electrochemical behavior.[33–36] There are few reports on Au^{3+} as the gold salt and few attention focused on the inhibition for black pad. During the electroless gold deposition, Au layer is usually produced by the controlled chemical reduction of metallic ions onto a catalytic surface. Therefore, the added reducing agent should be catalyzed by the substrate (*i.e.* nickel for our work) and the Au deposition is favored on it.[37] In electroless nickel plating baths, many reducing agents including sodium hypophosphite, amino boranes, sodium borohydride, and hydrazine have been shown to be catalyzed by nickel.[30] Because of its low-cost and relative safety, sodium hypophosphite is especially attractive in electroless nickel plating. Inspired by previous reports, low-cost and environment-friendly DMH and sodium hypophosphite were used as the complexing agent and reducing agent in our work, respectively.

In this study, a green and environmentally friendly cyanide-free gold plating bath was developed with adding hypophosphite as a reducing agent into the Au(III)–DMH based plating bath to retard the corrosion of Ni–P layer. At first, the structures and elemental compositions of Cu/Ni–P/Au coatings prepared from plating baths containing different concentrations of sodium hypophosphite were studied, including scanning electron microscope (SEM), X-ray diffraction (XRD), and X-ray photoelectron spectroscopy (XPS). Importantly, the corrosion resistance of the coatings was evaluated by salt spray tests, potentiodynamic polarization (PDP) tests, and electrochemical impedance spectroscopy (EIS) tests. It proved that the addition of sodium hypophosphite as a reducing agent into the Au(III)–DMH based plating bath improved the corrosion resistance of Cu/Ni–P/Au coatings efficiently. Finally, the catalytic process for the oxidation of hypophosphite was conformed by atomic absorption spectrophotometer (AAS) and quantum chemical calculations. Overall, this basic research showed the importance of reducing agents and great potential of using Au^{3+} as the main salt in electroless gold deposition. For developing the novel environmentally friendly cyanide-free Au(III) based plating bath, researchers can no longer limit their attention only to the development of cyanide-free complexing agents as usual, and the exploration of reducing agents is also particularly important for cyanide-free gold plating.

 © 2021 The Author(s). Published by the Royal Society of Chemistry

Open Access Article. Published on 08 December 2021. Downloaded on 2/7/2026 7:15:34 PM.
This article is licensed under a Creative Commons Attribution-NonCommercial 3.0 Unported Licence.

2. Material and methods

2.1 Reagent and electroless deposition of Cu/Ni–P/Au coatings

In this work, $AuCl_3$ was used as the gold salt, purchased from Macklin Biochemical Co., Ltd (China). DMH, NaH_2PO_2, NaH_2PO_4, Na_2HPO_4, $Na_2S_2O_8$, and $PdCl_2$ were obtained from Aladdin Bio-Chem Technology Co., Ltd (China). All the chemicals used were analytical grade. Ultrapure water (18.2 MΩ cm^{-1}) was employed as the solvent.

Copper sheets (see Fig. S1(a)† (ESI) for SEM image) were used as the substrates in this study. Copper sheets were degreased with a cleaner (9167T, GHTECH, China) for 5 min at 35 °C, subsequently pickled in a mixed solution of 5 wt% sulfuric acid and 60 g L^{-1} $Na_2S_2O_8$ for 1 min at room temperature (see Fig. S1(b)† (ESI) for SEM image) and activated in 30 mg L^{-1} $PdCl_2$ solution for 3 min at room temperature. After these pretreatment steps, copper sheets were immediately transferred into the commercial electroless Ni–P plating bath (5183S, GHTECH, China). Its compositions and operation conditions are presented in Table 1. The thickness and P content of the Ni–P layer (see Fig. S2(a)† (ESI) for SEM image) are 5 μm and 9.4 wt%, respectively. Electroless nickel plating was followed by electroless gold plating process. Detailed chemical composition and operation conditions of the electroless gold plating bath are listed in Table 2. In order to obtain the same thickness of Au layer, the operation time decreases with the increase of the concentration of NaH_2PO_2. The reaction time of gold plating process is listed in Table S1† (ESI). Unless otherwise specified, the thickness of the Au layer is 0.05 μm. There was a doubly distilled water washing step between each step of the process above.

2.2 Characterization

Thickness was measured by an X-ray coating thickness meter (XDLM-PCB200, Fischer, Germany). Surface morphologies of the Au layers and Ni–P layers after stripping gold were characterized through SEM (Phenom ProX, Phenom-World, Netherlands) with 15 kV accelerating voltage. Comparing with the SEM images (Fig. S2† (ESI)) of Ni–P layer before and after the stripping process, it can be seen that the surface morphology of the Ni–P layer has not changed significantly after the stripping step, indicating that the stripping process will not damage the Ni–P layer. The cross-sectional morphologies were analyzed by a field-emission scanning electron microscope (FESEM, LYRA 3 XMU, Tescan, Czech Republic) with a focused ion beam (FIB). To avoid the damage of the gold layer during sanding, a 5 μm Ni–P layer as a protective layer was deposited on the gold layer when making the sample for photographing the cross-sectional morphology. The composition of the nickel plating bath was the same as above. Atomic force microscopy (AFM, Dimension FastScan, Bruker, America) was used to obtain 3-D surface topography of the Ni–P layer. The crystal structure was investigated by performing X-ray diffraction (Aeris, Panalytical, Netherlands) using Cu Kα1 radiation and the identification of peaks on the XRD patterns was carried out by using the data of the card file JSPDS. The chemical composition of the Au layer was analyzed by X-ray photoelectron spectroscopy (Escalab 250Xi, Thermo Fisher, England) with a monochromatic Al Kα X-ray source and a beam diameter of 650 μm, operating at a pressure around 5.0×10^{-9} mBar. XPS depth profiles study was performed by etching the surface with a 1 keV Ar ion beam for 100 s repeatedly, and XPS spectra were taken after every etching cycle. The reference sputtering rate was 0.1 nm s^{-1}, as calibrated *vs.* a silicon dioxide standard. Due to the fluctuation of the coating surface, the etch depth did not represent the accurate coating thickness.

Corrosion tests included neutral salt spray tests, PDP tests, and EIS tests. The neutral salt spray tests were realized in the cyclic corrosion tester (LX-60A, Laibote, China). According to ISO 9227-2017 standard, the temperature and air pressure of the atomized saline solution were maintained at 35 °C and 197.2 kPa, respectively. The samples were exposed to a 5 wt% NaCl solution and retrieved for observation with naked eyes and optical microscopy after 48 hours. The electrochemical corrosion resistance of the Cu/Ni–P/Au coatings in a 3.5% NaCl solution was analyzed using an Autolab electrochemical work station (Pgstat302n, Metrohm, Switzerland) equipped with a three-chamber electrochemical cell. The working electrode was the Cu/Ni–P/Au coating with a square area of 0.7×0.7 cm^2, exposed in a 3.5 wt% NaCl solution for about 30 min before each experiment to stabilize the potential, which was then taken as the open circuit potential (OCP). A platinum electrode (Φ 16 mm) and saturated calomel electrode (SCE) were performed as the counter and reference electrodes, respectively. A lugging capillary was placed near the working electrode to reduce the IR drop. In PDP tests, the potential range was ±300 mV *vs.* the OCP with a scan rate of 5 mV s^{-1}. In EIS tests, the frequency region was from 10^5 to 0.05 Hz with a 10 mV amplitude in the OCP. The fitting results of PDP and EIS tests were obtained with the built-in software. The electrochemical parameters obtained from the PDP curves were used in the calculation of the total coating porosity (P):[38]

Table 1 Chemical composition of the electroless nickel plating bath and its operation condition

Chemicals	Concentration	Condition
$NiSO_4 \cdot 6H_2O$	21 g L^{-1}	pH = 4.8
NaH_2PO_2	28 g L^{-1}	Temperature: 85 °C
Others	Proprietary	Plating time: 25 min

Table 2 Chemical composition of the electroless gold plating bath and its operation condition

Chemicals	Concentration	Condition
$AuCl_3$	0.54 g L^{-1}	pH = 6.0
DMH	4.88 g L^{-1}	Temperature: 85 °C
NaH_2PO_2	0–10 g L^{-1}	Plating time: 8–15 min
$NaH_2PO_4 \cdot 2H_2O$	27.36 g L^{-1}	
Na_2HPO_4	3.49 g L^{-1}	

Open Access Article. Published on 08 December 2021. Downloaded on 2/7/2026 7:15:34 PM.
This article is licensed under a Creative Commons Attribution-NonCommercial 3.0 Unported Licence.

$$R_p = \frac{\beta_a \times \beta_c \times 10^6}{2.3 \times i_{corr} \times (\beta_a + \beta_c)}$$

$$P = \frac{R_{p(substrate)}}{R_{p(coating)}} \times 10^{-|\Delta E_{corr}/\beta_{a(substrate)}|}$$

where R_p is the polarization resistance, P is the total coating porosity, i_{corr} is the corrosion current density, E_{corr} is the corrosion potential, β_a and β_c are the anodic and cathodic Tafel slopes, respectively.

The adhesion properties of the coatings were determined by tape. First, the samples were stored in the high and low temperature cyclic tester (BPH-060C, Blue pard, China) for 16 days. A high temperature of 130 °C for 24 hours and a low temperature of −35 °C for 24 hours constituted a cycle. After being destroyed by extreme temperature, a blade was used to scratch 100 squares of 1 mm^2 on the coatings. Then stick on the transparent tape (600, Scotch, America) and tear off after pressing according to the standard ASTM D3359.

UV-vis absorption spectra were recorded on a spectrophotometer (Lambda 950, PerkinElmer, America) for investigating the stability of baths.

Atomic absorption spectrophotometer (AA-6800, Shimadzu, Japan) was used to detect the concentration of nickel ions in the solution.

2.3 Quantum chemical calculation

ORCA 4.2.1 program was employed for the quantum chemistry calculations.[39,40] All results presented in this work were calculated in the SMD solvation model[41] with water as solvent. Basis set of def2-SV(P)[42,43] was employed for geometry optimization with the PBE0-D3(BJ)[44,45] functional method. The structure analyses were performed *via* the Multiwfn 3.8(dev) code.[46] The molecular structure and isosurface maps were rendered by means of Visual Molecular Dynamics (VMD) software[47] based on the files exported by Multiwfn. The metal surface orientation was (111) facet.

3. Results and discussion

3.1 Structural characterization of Cu/Ni–P/Au coating

3.1.1. Macroscopic and microscopic morphologies of the Au layers. Five concentrations (0, 2.5, 5.0, 7.5, and 10 g L^{-1}) of NaH_2PO_2 were chosen to be added into the plating bath for gold deposition. Fig. 1 shows the SEM morphologies and macroscopic appearances of the obtained Au layers. In the absence and the presence of NaH_2PO_2, the appearances of the deposited gold were yellow, and there was no obvious difference. SEM images showed that the deposited Au layers consisted of nodules about 1–2 μm in diameters, and different concentrations of NaH_2PO_2 had no significant effect on nodule size. This structure was consistent with that typically observed for Au layer deposited by electroless method.[32,36,48] Through further observation, the microscopic difference of the Au layers deposited with different concentrations of NaH_2PO_2 can be found. As shown in Fig. 1(a), many micropores appeared in the Au layer deposited without NaH_2PO_2, and their sizes were about 0.15–0.4 μm. These micropores may be the reaction channels left by the intense attack of Au^{3+} to the Ni–P layer. The micropores will also become the channels for the penetration of corrosive medium, which are unfavorable to the corrosion resistance of coatings.[49] For adding the concentration of 2.5 g L^{-1} NaH_2PO_2, the numbers and sizes (about 0.08 μm) of micropores decreased significantly. With the increase of the added concentration of NaH_2PO_2, the appearances of the Au layers developed further better. As shown in Fig. 1(d), the micropores on the Au layer were almost invisible. Thus it can be concluded that the addition of NaH_2PO_2 is beneficial to obtain a dense Au layer.

3.1.2. Microscopic morphologies of the Ni–P layers after stripping Au. Black pad is one of the most concerned problems in ENIG process. Even in the cyanide system, it is hard to avoid the black pad. In order to assess the extent of the black pad, it is

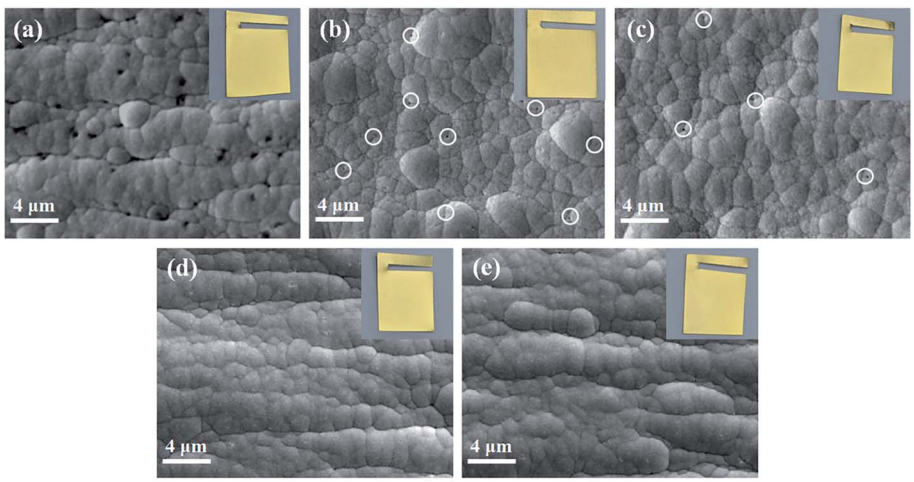

Fig. 1 SEM images of the Au layers deposited from cyanide-free baths containing different concentrations of NaH_2PO_2: (a) 0 g L^{-1}, (b) 2.5 g L^{-1}, (c) 5.0 g L^{-1}, (d) 7.5 g L^{-1}, and (e) 10 g L^{-1}. The inset images are the macroscopic appearances.

 © 2021 The Author(s). Published by the Royal Society of Chemistry

Open Access Article. Published on 08 December 2021. Downloaded on 2/7/2026 7:15:34 PM.
This article is licensed under a Creative Commons Attribution-NonCommercial 3.0 Unported Licence.

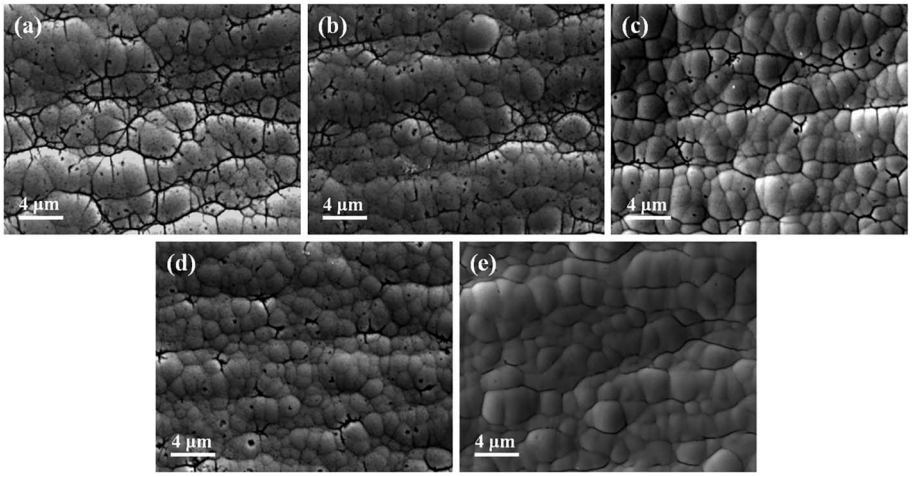

Fig. 2 SEM images of the Ni–P layers after stripping the Au layer prepared from cyanide-free baths containing different concentrations of NaH_2PO_2: (a) 0 g L^{-1}, (b) 2.5 g L^{-1}, (c) 5.0 g L^{-1}, (d) 7.5 g L^{-1}, and (e) 10 g L^{-1}.

usual to observe the microscopic morphologies of Ni–P layer after stripping Au. Fig. 2 shows the SEM images of the Ni–P layers after stripping the Au layers prepared with different concentrations of NaH_2PO_2. It is obvious that the Ni–P layers were also a nodular structure. As we have mentioned in the introduction, serious nickel corrosion is inevitable if the Au layer deposits in the form of immersion, and this is confirmed as shown in Fig. 2(a). Extensive fissures between the nodules and a few pitting corrosion were clearly observed in Fig. 2(a), meaning that the Ni–P layer was seriously damaged.[50] Similar to the micropores in the Au layer, these fissures and pitting may also become channels for corrosive media. The P content of Ni–P layer is the main factor controlling its corrosion resistance. However, the distribution of P in the plane and depth directions is usually uneven, especially at nodule boundaries, where the P content is lower, causing Ni–P layer to be preferentially corroded by Au^{3+}.[51–53] Therefore, it can be seen that corrosion mainly occurred at the boundaries. After adding NaH_2PO_2 into the bath, the corrosion degree was mitigated, which was in line with our expectations. In Fig. 2(d), it can be seen that the length of the fissures had become partial and short, while in Fig. 2(e), the fissures could hardly be seen, which proves the essential role of NaH_2PO_2 in Au(III) based cyanide-free electroless gold plating bath. The mechanism of nickel corrosion has rarely been studied, and some researchers believed that it was related to the formation of galvanic cells in areas with different P content in Ni–P layer.[54] Regardless of the specific mechanism, the direct cause of nickel corrosion is the displacement reaction between gold ions and nickel atoms. The addition of NaH_2PO_2 could replace the role of nickel atoms and donate electrons to Au^{3+}; therefore the black pad phenomenon was reduced. Fig. 2 reveals that as the concentration of NaH_2PO_2 increased, this substitution effect become more pronounced.

3.1.3. Cross-sectional morphologies of the Cu/Ni–P/Au coatings. Cross-sectional SEM analyses of the Cu/Ni–P/Au coatings are shown in Fig. 3. It can be seen from Fig. 3(a) that the spikes penetrated into the Ni–P layer with a depth of about 0.62–2.19 μm, which was a conclusive evidence of the black pad. At the same time, the Ni–P layer was deformed and become a bulging shape due to the attack of Au^{3+}, which was also

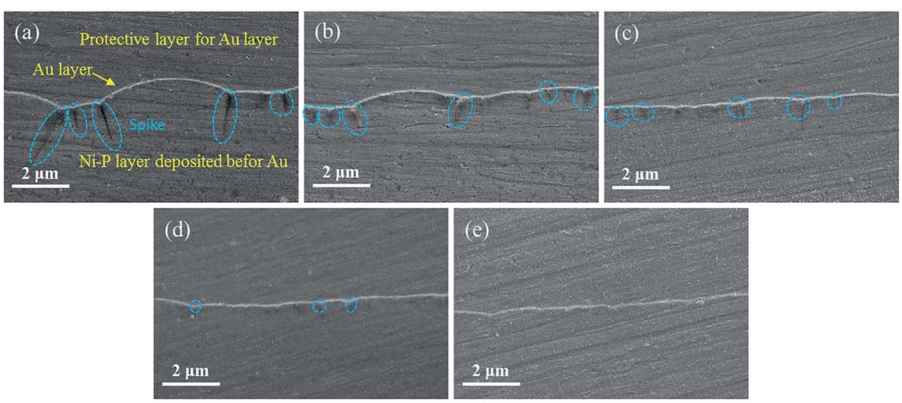

Fig. 3 Cross-sectional SEM images of the Cu/Ni–P/Au coatings deposited from cyanide-free baths containing different concentrations of NaH_2PO_2: (a) 0 g L^{-1}, (b) 2.5 g L^{-1}, (c) 5.0 g L^{-1}, (d) 7.5 g L^{-1}, and (e) 10 g L^{-1}.

Open Access Article. Published on 08 December 2021. Downloaded on 2/7/2026 7:15:34 PM.
This article is licensed under a Creative Commons Attribution-NonCommercial 3.0 Unported Licence.

common in black pad.[31,50] In the presence of NaH_2PO_2, the depths of the spikes were reduced. As shown in Fig. 3(b–d), the depths of the spikes were 1.0, 0.5, and 0.2 μm, respectively, corresponding to the NaH_2PO_2 concentrations of 2.5, 5.0, and 7.5 g L^{-1}. 0.2 μm spikes were generally acceptable in actual application. With adding the 10 g L^{-1} NaH_2PO_2, it is worth noting that there was no spike observed in Fig. 3(e) and the Au layer was relatively flat. The cross-sectional morphologies of the coatings also indicate that adding NaH_2PO_2 as a reducing agent into the Au(III)–DMH based plating bath is beneficial to inhibit the occurrence of black pad.

3.1.4. Crystal structures of the Cu/Ni–P/Au coatings. The crystal structures of the Cu/Ni–P/Au coatings obtained with different concentrations of NaH_2PO_2 were examined *via* XRD. Fig. 4 displays the overlaid diffractions of the coatings. It can be seen that the crystal structure and composition in different coatings were agreed well with others reports about electroless gold plating.[48,55,56] Copper peaks were present at $2\theta = 43.7°$, 50.8°, and 74.4° due to the copper substrate, and the very broad peaks at 44.7° were ascribed to the (111) of amorphous Ni–P alloy.[57] The Au (111), Au (220), and Au (300) diffraction peaks were detected at 38.6°, 65.1°, and 78.0°, respectively, and the Au (111) was the preferred orientation. The XRD patterns of the gold peaks of five kinds of coatings were similar, indicating that the addition of NaH_2PO_2 did not affect the crystal structure of gold regardless of the NaH_2PO_2 concentration. In the electroless nickel plating process using NaH_2PO_2 as the reducing agent, the deposited nickel layer is a nickel–phosphorus alloy instead of pure nickel. The P element is derived from NaH_2PO_2, and its content in Ni–P layer is positively correlated with the concentration of NaH_2PO_2.[53] The co-deposition of P in the crystal lattice of the nickel layer leads to structure distortion, disrupting of periodicity, and hence formation of a crystalline coating.[58,59] Crystalline, mixed amorphous crystalline, and amorphous structures of the Ni–P layers were different for low (1–5 wt%), medium (5–9 wt%), and high (>9 wt%) phosphorus content, respectively.[53] In this work, NaH_2PO_2 was also adopted for electroless gold plating, so it is inevitable to be confused about the question for whether P element being co-deposited? According to the results from Fig. 4 that the diffraction peaks of the Au(111) did not broaden significantly, we can speculate preliminarily that there was no P element in the Au layers, or the P content was so low that it was not enough to create an arresting change in the crystal structures. The exact P content requires further analysis.

3.1.5. Elemental composition of the Au layers. XPS as a surface analysis technology was used to confirm the elemental composition of the Au layer. Since the detection depth in XPS is less than 10 nm, the P element in the Ni–P layer will not be monitored, which is very suitable for studying the elements in the Au layer. Fig. 5 shows the full XPS spectrum of the Au layer (0.09 μm) before and after etching 10 nm. As the Au layer was mainly composed of Au, the Au peaks were very obvious. Before etching, polluting elements C and O were detected, probably from the atmospheric environment, as they disappeared after etching. The inset image shows the high-resolution XPS spectrum of P 2p region, and no peak was observed. The XPS analysis indicated that the Au layer did not contain P element, and the Au layer was pure gold.

The valence state of P in NaH_2PO_2 is +1, therefore, it may be accompanied by an oxidation reaction (+1 → 0) when being oxidized (+1 → +3 or +1 → +5), but it is worth noting that it is not inevitable. For example, in the treatment of electroless nickel plating wastewater containing NaH_2PO_2, hypophosphite

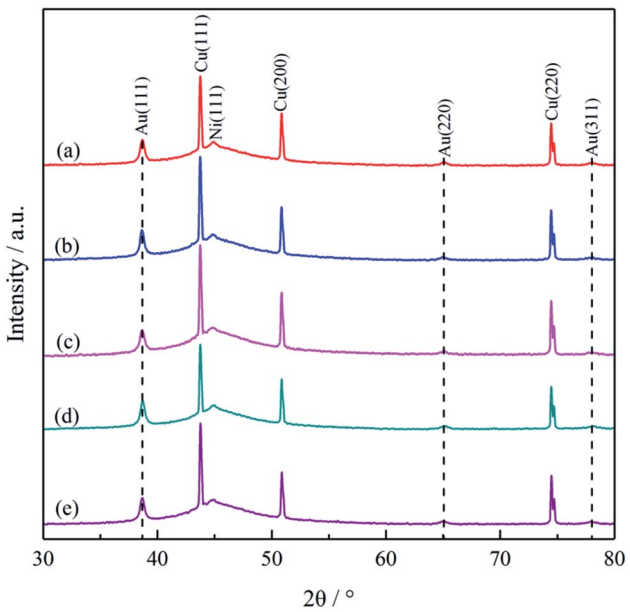

Fig. 4 XRD patterns of Cu/Ni–P/Au coatings deposited from cyanide-free baths containing different concentrations of NaH_2PO_2: (a) 0 g L^{-1}, (b) 2.5 g L^{-1}, (c) 5.0 g L^{-1}, (d) 7.5 g L^{-1}, and (e) 10 g L^{-1}.

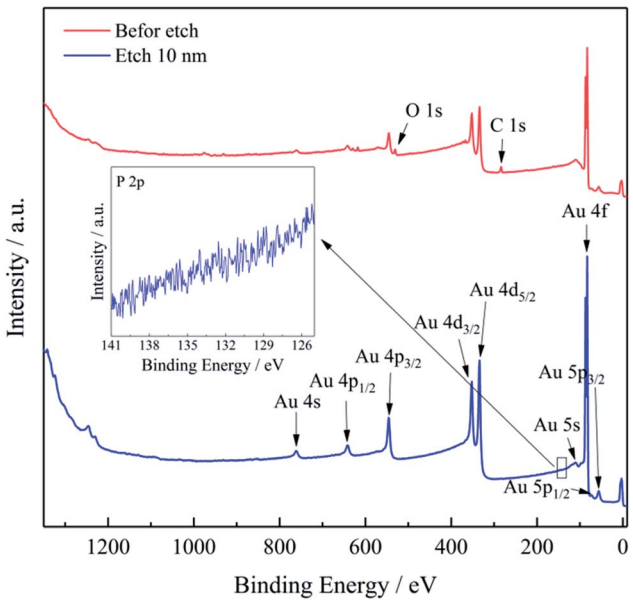

Fig. 5 Full XPS spectrum of the Au layer before and after etching 10 nm. The inset image is the high-resolution XPS spectrum of P 2p region.

 © 2021 The Author(s). Published by the Royal Society of Chemistry

Open Access Article. Published on 08 December 2021. Downloaded on 2/7/2026 7:15:34 PM.
This article is licensed under a Creative Commons Attribution-NonCommercial 3.0 Unported Licence.

was oxidized to phosphate for recovery, and no phosphorus (0 valence state) was detected in the precipitates.[60] In the field of metal deposition, the necessary condition for the formation of alloys is that the electrode potentials of the co-deposited elements are close according to the co-deposited theory. Reduction potentials for Ni^{2+}/Ni ($E = -0.594$ V *vs.* NHE) and $H_2PO_2^-$/P ($E = -0.714$ V *vs.* NHE) are near relatively facilitating their codeposition.[53,61,62] However, the situation of Au^{3+} is quite different from that of Ni^{2+}. The reduction potential for $Au(DMH)_4^-$/Au ($E = -0.276$ V *vs.* NHE) is much higher than that of $H_2PO_2^-$/P, so it is difficult to co-deposit Au with P to form alloy in principle.[28] Since the electrode potential of $Au(DMH)_4^-$/Au is higher than that of $H_2PO_2^-$/P, Au deposits preferentially at first. Therefore, the Au layer was pure gold with no containing P element, and the XPS results eliminated the confusion about whether P co-deposited with Au.

XPS depth profiles (see Fig. 6) provide more abundant element distribution information of the coating, which is favorable to understand the process of deposition mechanism. When the etching depth was less than 50 nm, there were only Au 4f peaks, but no Ni 2p, P 2p, or O 1s peaks was observed, which also indicated that the Au layer (~50 nm) was pure gold. After

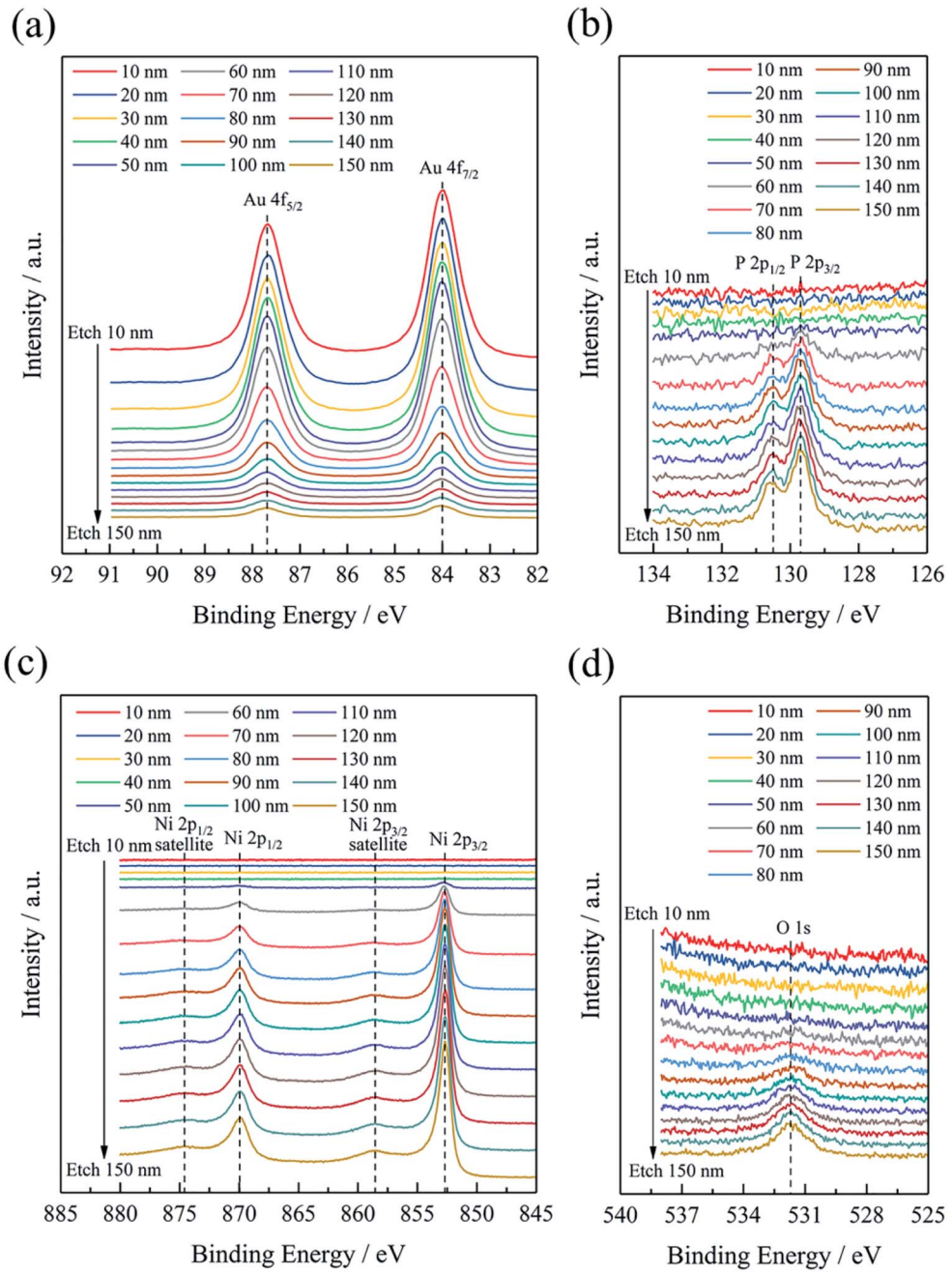

Fig. 6 High-resolution XPS spectra of (a) Au 4f, (b) Ni 2p, (c) P 2p, and (d) O 1s with different etch depth.

Open Access Article. Published on 08 December 2021. Downloaded on 2/7/2026 7:15:34 PM.
This article is licensed under a Creative Commons Attribution-NonCommercial 3.0 Unported Licence.

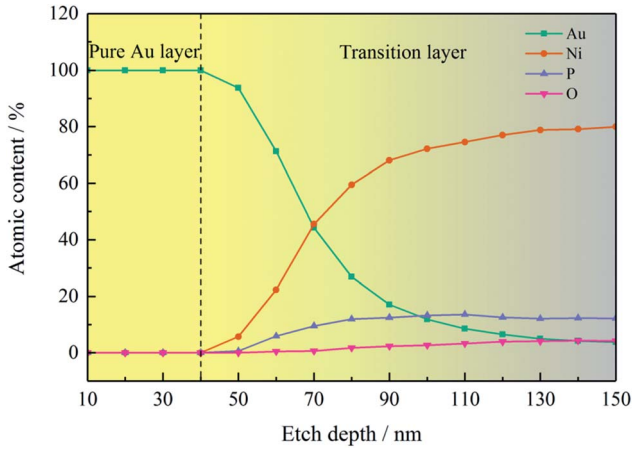

Fig. 7 Elemental contents of Au, Ni, P, and O obtained from depth profiles.

etching depth above 50 nm, an interesting result was detected that the intensities of Au 4f peaks gradually decreased, while the intensities of Ni 2p, P 2p, and O 1s peaks increased. And it is obvious that there appeared the defined region where the four elements coexisted after etching 50 nm. With the increase of etching depth, the Au content decreased while the other three elements increased. High-resolution Ni 2p XPS spectra exhibited four deconvoluted peaks (Fig. S3† (ESI)), corresponding to Ni, NiO, and Ni–P, in agreement with the compositions of Ni–P layer.[15] The variation of element content with different etching depth is shown in Fig. 7, and the detailed values are listed in Table S2† (ESI). The O element was possibly introduced into the Ni–P layer from the washing step after the electroless nickel plating. Therefore, it can be seen from Fig. 7 that O element appeared at the same time as the Ni and P elements, reflecting the composition of the oxidized Ni–P layer. After etching

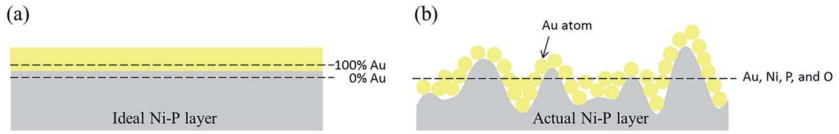

Fig. 8 Schematic diagrams of deposition process of gold particles in the early stage on (a) ideal Ni–P layer and (b) actual Ni–P layer.

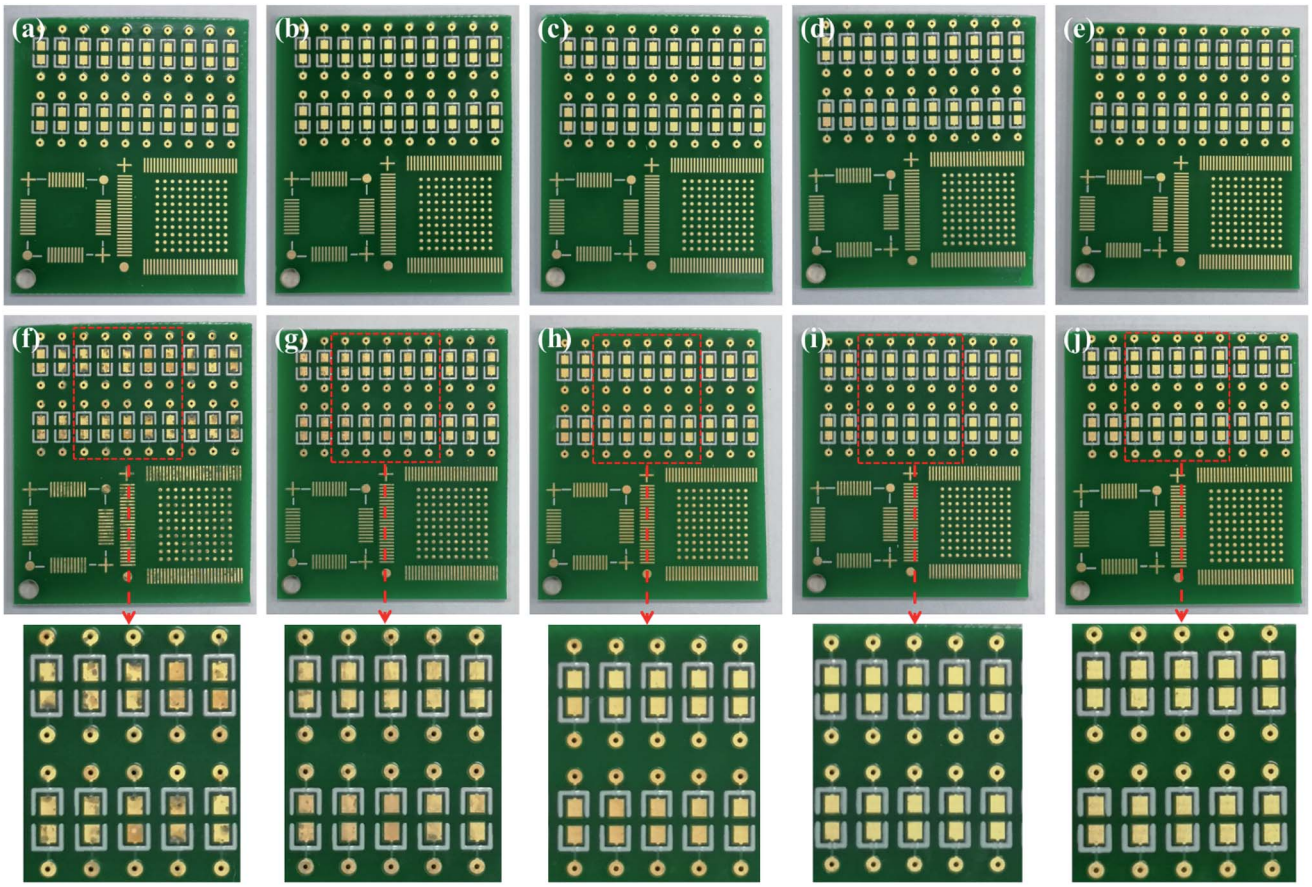

Fig. 9 Appearances of printed circuit board before (a–e) and after (f–j) salt spray tests. The Au layers were deposited from cyanide-free baths containing different concentrations of NaH_2PO_2: (a and f) 0 g L^{-1}, (b and g) 2.5 g L^{-1}, (c and h) 5.0 g L^{-1}, (d and i) 7.5 g L^{-1}, and (e and j) 10 g L^{-1}.

 © 2021 The Author(s). Published by the Royal Society of Chemistry

Open Access Article. Published on 08 December 2021. Downloaded on 2/7/2026 7:15:34 PM.
This article is licensed under a Creative Commons Attribution-NonCommercial 3.0 Unported Licence.

150 nm, there was still 3.81 at% Au coexisting with the Ni–P layer. It can be found that although the deposited Au layer was pure gold, the gold in the early stage seemed to integrate with the Ni–P layer. The thickness of this special area cannot be underestimated, which is thicker than the pure gold layer in the strict sense. The formation of this special area is closely related to the nodular structure of the Ni–P layer. If the surface of the Ni–P layer was completely flat, gold particles should uniformly deposit on it, as shown in Fig. 8(a). At this time, XPS depth profiles should show that the Au content changes from 100% to 0%. However, the surface of the Ni–P layer was not as ideal as we imagined in fact. As shown in the AFM image of the Ni–P layer and the sectional analysis of the AFM image (Fig. S4† (ESI)), it looked like mountains with peaks and saddles. Gold will deposit on "saddles", gradually filling the spaces between the two "mountains", forming an inlaid structure with the Ni–P layer, as shown in the schematic diagram of Fig. 8(b). When etching to the Ni–P layer, the four elements of Au, Ni, P, and O will be detected at the same time. This special area can be considered as the transition layer between pure Ni–P layer and pure Au layer. The formation of the inlaid structure is very important to ensure the close combination of the two layers with different compositions. As mentioned in Section 2, the copper sheets needed to be soaked in a mixed solution of sodium thiosulfate and sulfuric acid for 1 minute before electroless nickel plating. As we all know, the purpose of this step is to form a concave–convex structure on the copper surface, then form an inlaid structure with the Ni–P layer to increase their contact area and improve their adhesion. It is foreseeable that the adhesion between the Au layer and the Ni–P layer will be qualified. Adhesion tests will be mentioned below.

3.2 Performances of the Cu/Ni–P/Au coatings

3.2.1. Corrosion tests. The atmospheric corrosion and oxidation of electronic circuits will lead to premature failure of electronic devices and reduce the service life of electronic products. In order to increase the corrosion resistance, gold with stable chemical properties is selected as the protective layer, while the nickel layer acts as a barrier between the Cu substrate and the Au layer to prevent atomic diffusion.[3] Of course, the Ni–P layer also has a protective effect on the Cu substrate.

The results of salt spray tests on the printed circuit boards are shown in Fig. 9, and Fig. 9(a–e) shows the appearances before the salt spray test. Similar to Fig. 1, there was no difference in the macroscopic appearances of the Au layers. Whether it was a large pad (Φ 1.47 mm) or a small one (Φ 0.57 mm), or a slender circuit (M = 0.25 mm), the yellow Au layer was successfully deposited on the Ni–P layer without omission. After 48 hours of salt spray corrosion, the appearances of the printed circuit boards are shown in Fig. 9(f–j). Compared with Fig. 9(a and f), a large number of brown stains appeared on the surface of the Au layer deposited from the bath without containing NaH_2PO_2, indicating that the coating has been corroded very seriously. Although gold is an inert metal, the inevitable gaps between the gold particles make it easy for the corrosive medium (Cl^-) to penetrate into the substrate. At the initial stage, the Ni–P layer was corroded due to the porous Au layer (Fig. 1(a)). With the corrosion of Cl^-, galvanic corrosion started where Au acted as the cathode and Ni as the anode.[50,63] Then Cl^- continued to penetrate into the Cu substrate through the wide boundary of the Ni–P layer (Fig. 2(a)), and Ni was accelerated to be corroded through galvanic coupling with Cu. Meanwhile, Cu used the defects of the Ni–P layer and Au layer to diffuse to the Au-top surface, and it was eventually oxidized there under the acceleration of a galvanic coupling with Au.[2] Murugan's research work[63] showed that the brown corrosion product was consisted of a thick base of Cu_2O covered by a film of CuO (major) and $Cu_2(OH)_3Cl$ (minor) with XPS analysis. It can be seen that the pores and gaps of the coating are closely related to corrosion resistance. It is noteworthy that the corrosion resistance of the coating enhanced remarkably after adding 2.5 g L^{-1} NaH_2PO_2 into the bath (see Fig. 9(g)). And with the further increase of concentration of added NaH_2PO_2, no brown stains could be observed clearly on the surface of boards, as shown in

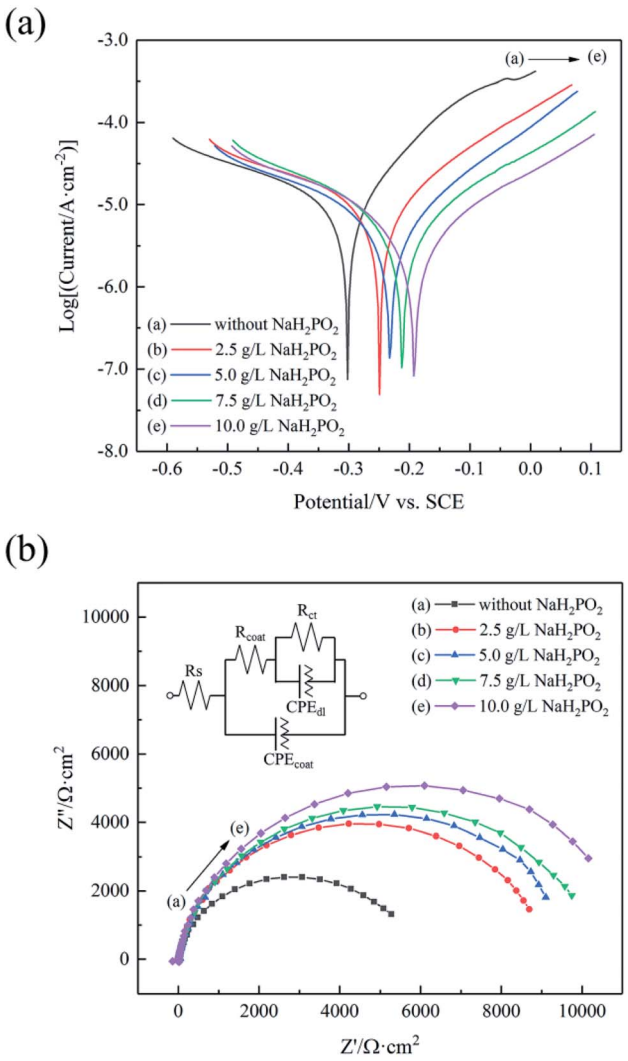

Fig. 10 (a) PDP curves and (b) Nyquist curves of the coatings in a 3.5 wt% NaCl solution. The inset image in (b) is the equivalent circuit.

Open Access Article. Published on 08 December 2021. Downloaded on 2/7/2026 7:15:34 PM.
This article is licensed under a Creative Commons Attribution-NonCommercial 3.0 Unported Licence.

Table 3 Electrochemical parameters for PDP tests and EIS tests in a 3.5 wt% NaCl solution

Sample	Concentration of NaH_2PO_2 (g L^{-1})	E_{corr} (V)	i_{corr} (μA cm^{-2})	β_a (V dec^{-1})	β_c (V dec^{-1})	P (%)	R_{ct} (kΩ cm^{-2})
Cu substrate	—	−0.329	26.6	0.120	0.403	—	—
Cu/Ni–P/Au coating	0	−0.302	11.5	0.163	0.407	20.53	5.83
	2.5	−0.248	8.0	0.344	0.178	5.05	9.01
	5.0	−0.231	5.9	0.336	0.192	2.58	9.99
	7.5	−0.217	5.5	0.303	0.237	1.70	10.33
	10.0	−0.191	4.6	0.295	0.251	0.84	11.31

Fig. 9(h–j). The optical microscope images also show that the addition of NaH_2PO_2 is beneficial to the salt spray corrosion resistance of the coatings, as shown in Fig. S5† (ESI). Combined with the SEM images in Fig. 1–3, it can be concluded that the obtained dense Ni–P/Au coatings deposited after adding NaH_2PO_2 retard the corrosion of the printed circuit boards.

The PDP curves of the coatings deposited in the baths containing different concentrations of NaH_2PO_2 are shown in Fig. 10(a), and the corresponding parameters are summarized in Table 3. Generally speaking, corrosion potential (E_{corr}) is a thermodynamic parameter indicating the corrosion trend, and corrosion current density (i_{corr}) is a kinetic parameter indicating the corrosion rate.[64] A high E_{corr} means that corrosion reaction is difficult to occur, and a low i_{corr} means that the corrosion rate is low. In the absence of NaH_2PO_2, the coating exhibited a low E_{corr} (−0.302 V) with a high i_{corr} (11.5 μA cm^{-2}). As the concentration of added NaH_2PO_2 gradually increased from 2.5 g L^{-1} to 10 g L^{-1}, the E_{corr} of four coatings increased and i_{corr} decreased slightly. When the added NaH_2PO_2 concentration was 10 g L^{-1}, the obtained coating exhibited the highest E_{corr} (−0.191 V) and the lowest i_{corr} (4.6 μA cm^{-2}). The corrosion resistance in our investigation is better than the Cu/Ni–P/Au coating deposited from an Au(I)–sulfite–thiosulfate bath reported in the literature[55] ($E_{corr} = -0.278$ V and $i_{corr} = 5.8$ μA cm^{-2}). We speculate that this difference may stem from denser Au and Ni–P layers in our work. Unfortunately, the morphology of the Ni–P layer after stripping off gold was not shown in the literature.[55] In addition, the comparison of the porosity of different Ni–P/Au coatings was listed in Table 3. The PDP curve for copper is shown in Fig. S6† (ESI), and it is used to obtain electrochemical parameters (substrate) for porosity calculation. It can be seen from Fig. 1 and 2 that the porosity is more related to the fissure of Ni–P layer than the micropore of Au layer, because there are more defects (fissure and pitting) in Ni–P layer. It is clear that the porosity of the coatings decreased with the increase of the concentration of added NaH_2PO_2. The coating obtained from the bath with 10 g L^{-1} NaH_2PO_2 had the lowest porosity (0.84%), which was significantly lower than that without NaH_2PO_2 (20.53%), indicating that the addition of NaH_2PO_2 not only makes Au layer more dense, but also reduces the defects of Ni–P layer.

Fig. 10(b) displays the Nyquist curves and corresponding equivalent circuit of the coatings in a 3.5 wt% NaCl solution. The Nyquist plots of all coatings show imperfect semicircles (incomplete capacitor arcs), indicating the existence of a single low-frequency capacitor arc in the frequency range studied.[65] In general, the larger the diameter of the semicircle, the better the corrosion resistance.[66] From the Nyquist curves, it can be preliminarily judged that after NaH_2PO_2 was added, the corrosion resistance of the coating was improved, as the diameter

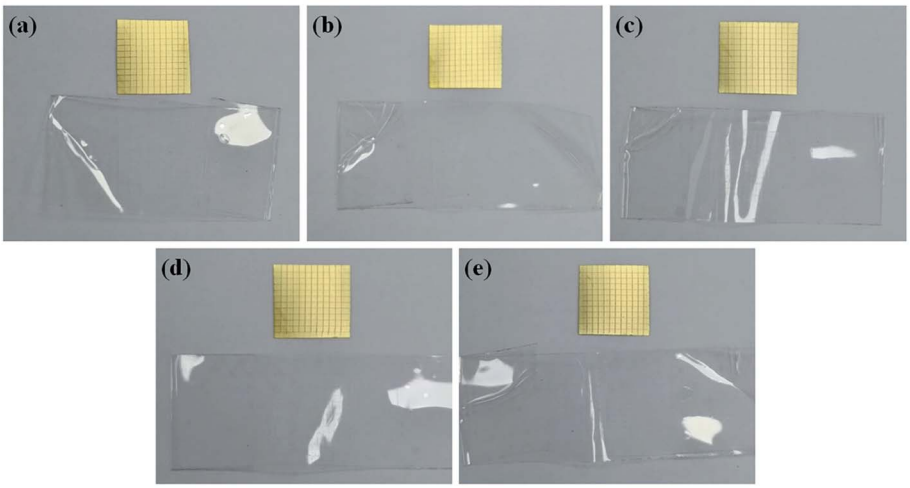

Fig. 11 Appearances of Au layers and tape after adhesion tests. The Au layers were deposited from cyanide-free baths containing different concentrations of NaH_2PO_2: (a) 0 g L^{-1}, (b) 2.5 g L^{-1}, (c) 5.0 g L^{-1}, (d) 7.5 g L^{-1}, and (e) 10 g L^{-1}.

 © 2021 The Author(s). Published by the Royal Society of Chemistry

Open Access Article. Published on 08 December 2021. Downloaded on 2/7/2026 7:15:34 PM.
This article is licensed under a Creative Commons Attribution-NonCommercial 3.0 Unported Licence.

increased successively. For the qualitative interpretation of the Nyquist curves, an equivalent circuit was selected to perform curves fitting. R_s presents the solution resistance, R_{coat} is the coating resistance, and R_{ct} is the charge transfer resistance. CPE_{coat} is a constant phase element, which represents the capacitance of the coating. CPE_{dl} is the double-layer capacitance.[67] The corrosion resistance of a coating is positively related to R_{ct}. Bode phase plots (Fig. S7† (ESI)) give two peaks at investigated frequency range which indicate the presence of two time constants. The one in the high-frequency can be represented by R_{coat} and CPE_{coat}. The one in the lower-frequency range is attributed to the corrosion reactions, which are elucidated by the R_{ct} and CPE_{dl}.[68] The values of R_{ct} are listed in Table 3, and other fitting parameters are summarized in Table S3† (ESI). The results in Table 3 show that as the concentration of NaH_2PO_2 increased, R_{ct} increased prominently from 5.83 kΩ cm^{-2} to 11.31 kΩ cm^{-2}. The results obtained from the EIS tests are in accordance with those from the salt spray tests and the PDP tests. The corrosion resistance of the Cu/Ni–P/Au coating

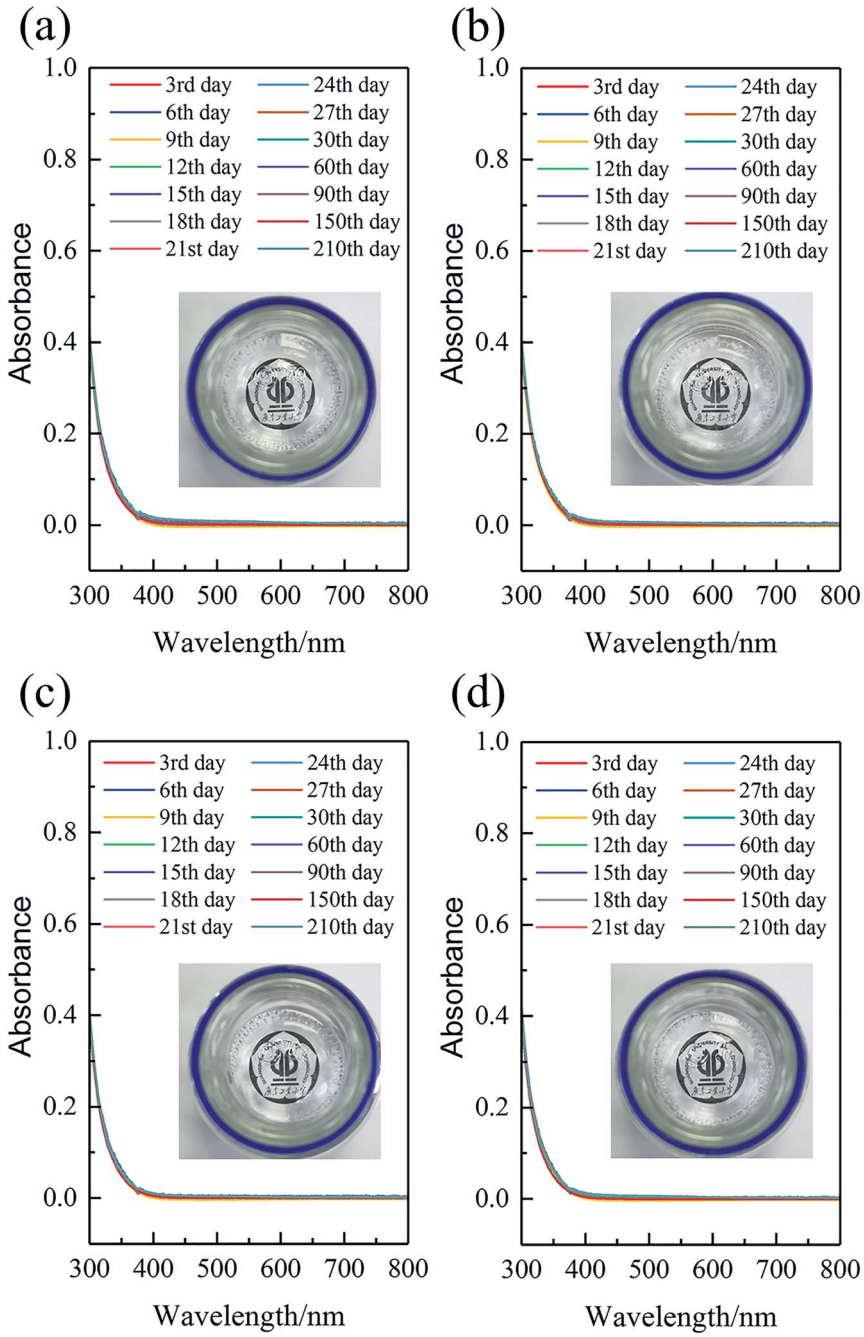

Fig. 12 Evolution of the UV-vis absorption curves of the cyanide-free bath containing different concentrations of NaH_2PO_2 over 210 days: (a) 2.5 g L^{-1}, (b) 5.0 g L^{-1}, (c) 7.5 g L^{-1}, and (d) 10 g L^{-1}. The inset images are the top view of the baths after 210 days.

Open Access Article. Published on 08 December 2021. Downloaded on 2/7/2026 7:15:34 PM.
This article is licensed under a Creative Commons Attribution-NonCommercial 3.0 Unported Licence.

can be improved significantly with adding NaH_2PO_2 as the reduction agent in Au(III)–DMH based cyanide-free plating bath.

3.2.2. Adhesion tests. Adhesion is another important performance for coatings. A coating with poor adhesion property will fall off easily and lose the significance of protection. Fig. 11 displays the appearances of the Au layers and the tapes after adhesion tests. As shown in Fig. 11, there were no signs of detachment on the Cu/Ni–P/Au coatings regardless of the presence of NaH_2PO_2 after extreme temperature destruction and tape sticking. The result shows that the adhesion of the coating was qualified and could be classified as 5B level according to the standard ASTM D3359. The effective adhesion performance of the Au layer is related to the inlaid structure formed in the interface between the Au layer and the Ni–P layer shown in XPS depth profiles.

3.3 Characterization of the stability of gold plating bath

The unsatisfactory bath stability both for Au(I) and Au(III)-reductant based cyanide-free electroless gold plating remains challenging in electroless deposition. With the addition of NaH_2PO_2, the corrosion resistance of the coatings was improved, but the baths become metastable systems as the oxidation–reduction reaction between Au^{3+} and $H_2PO_2^-$ might occur in the solution. If the reaction occurs, the produced gold nanoparticles which present different colors with different particle sizes will result in the decomposition of the gold plating bath and the color of the bath will change.[69] Therefore, how to inhibit the oxidation–reduction reaction between Au^{3+} and $H_2PO_2^-$ in the solution is crucial in the presence of $H_2PO_2^-$. In this work, with adjusting the contents ratio of hypophosphite and complexing agent DMH as well as the plating process parameter, the good plating bath whose composition and operation condition are listed in Table 2 can retain good stability.

In the NaH_2PO_4–Na_2HPO_4 buffer system, after $AuCl_3$ coordinated with sufficient DMH, the prepared gold plating baths were colorless and transparent with the added NaH_2PO_2 concentration no more than 10 g L^{-1}. Furthermore, the baths remained colorless and transparent during storage for 210 days, as shown in inset images of Fig. 12. Also, the UV-vis absorption spectra (Fig. 12) of the plating baths were detected to access the bath stability. The observed absorption value of the baths in the visible region (about 400–800 nm) almost was unchanged and remained at constant (changed absorbance was less than 0.01). No new absorption peak appeared in the visible region, indicating that no gold nanoparticles formed during storage for 210 days.

In our previous work,[18] we reported the stability of Au(I)–DMH based immersion gold plating bath, that precipitated gold particles could be observed obviously after storage for 200 days at room temperature. However, in this work, the Au(III)–DMH based cyanide-free plating bath was more stable than Au(I)–DMH immersion bath, even adding NaH_2PO_2 as the reduction agent. The bath stability of Au(III)–DMH is inseparable from the stable nature of Au^{3+} ion itself which is not easy to disproportionate, and also from the stable nature of Au(III)–DMH complex

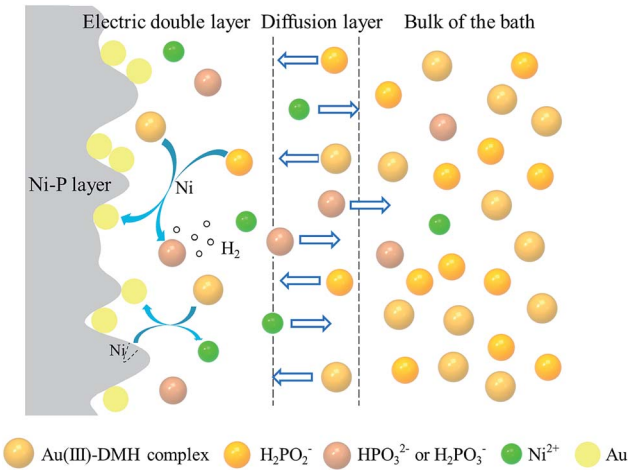

Fig. 13 Reaction diagrams on Ni–P layer in the electroless gold plating bath.

combined with the strong coordinated bonds. Of course, the contents of hypophosphite, plating process parameters, and the preparation method of baths are all related to bath stability. It is important that NaH_2PO_2 is added in portions to the bath finally.

3.4 Deposition process of the gold layer

In order to further learn about the deposition process, the produced concentration of Ni^{2+} ions at different reaction time in the two baths (without NaH_2PO_2 and with adding 10 g L^{-1} NaH_2PO_2) were detected by AAS, as shown in Fig. S8† (ESI). During the electroless gold plating process, the replacement reaction between Ni and Au(III)–DMH complex was certain to occur, therefore the concentration of Ni^{2+} both in the two baths increased with the increase of the reaction time. However, after adding NaH_2PO_2 into the bath, at the same deposition time, the concentration of produced Ni^{2+} decreased accordingly, indicating that NaH_2PO_2 as a reduction agent participated in the electroless deposition reaction. And the replacement reaction between Ni and Au(III)–DMH complex was replaced partly with the reduction reaction between $H_2PO_2^-$ and Au(III)–DMH complex. Combining Table S1† (ESI) and Fig. S8† (ESI), we calculated that the concentration of Ni^{2+} produced in the Au(III) based bath containing 10 g L^{-1} NaH_2PO_2 was about two-seventh of that of the Au(III) based immersion plating bath when depositing 0.05 μm gold layer, which was also lower than that of the Au(I) based immersion plating bath theoretically according to eqn (1) and (2).

As mentioned earlier, the replacement reaction of gold ions and nickel atoms during ENIG process leads to the unavoidable corrosive behavior of Ni–P layer, and the black pad phenomenon will occur if the corrosion of gold ions is serious. Though adding NaH_2PO_2 into the bath as a reduction agent, NaH_2PO_2 replaced nickel atom partially to provide electrons and participated in deposition reaction, and the corrosive resistance of Cu/Ni–P/Au coating enhanced as expected. In addition, the enriching of NaH_2PO_2 could also increase the deposition rate. The time required to deposit the same thickness of Au layers is

 © 2021 The Author(s). Published by the Royal Society of Chemistry

Open Access Article. Published on 08 December 2021. Downloaded on 2/7/2026 7:15:34 PM.
This article is licensed under a Creative Commons Attribution-NonCommercial 3.0 Unported Licence.

listed in Table S1† (ESI). The reduced deposition time will be beneficial for retarding the corrosion to Ni–P layer. In a word, NaH_2PO_2 as a reduction agent mitigates the attack of Au^{3+} on Ni–P layer by reducing the reaction time and retarding the occurrence of the replacement reaction.

Based on the related experiments and analysis, we proposed the gold deposition process, as shown in Fig. 13. In the bulk of the bath, the electrode potential of the complex formed by the coordination of DMH and Au^{3+} is lower than that of free Au^{3+} ions, and the reducing ability of $H_2PO_2^-$ is not enough to reduce the complex, so the plating bath can remain stable. The concentrations of Au(III)–DMH complex and $H_2PO_2^-$ in the bulk of the bath are higher than that on the Ni–P surface, so they will spontaneously diffuse to the Ni–P surface and adsorb on it to form an electric double layer. After $H_2PO_2^-$ adsorbs on the Ni–P surface, it is catalyzed by Ni, and the reduction ability is significantly improved, so the deposition reaction of gold occurs, which reflects the characteristics of substrate catalysis. Combined with XPS analysis, atomic hydrogen mechanism[30,51] of $H_2PO_2^-$ oxidation in nickel plating process, as well as our observation of gas (H_2 (ref. 70)) generation, we supposed the reaction equations of Au^{3+} and $H_2PO_2^-$:

$$H_2PO_2^- + H_2O \rightarrow H^+ + HPO_3^- + 2H_{ads} \quad (3)$$

$$Au^{3+} + H_{ads} \rightarrow Au + 3H^+ \quad (4)$$

$$2H_{ads} \rightarrow H_2 \quad (5)$$

where H_{ads} is the hydrogen atom in the adsorbed state. Electrochemical mechanism[30] is also a widely accepted oxidation mechanism of hypophosphite. The reaction equations of Au^{3+} and $H_2PO_2^-$ proposed by this mechanism are as follows:

$$H_2PO_2^- + H_2O \rightarrow 2H^+ + H_2PO_3^{2-} + 2e^- \quad (6)$$

$$Au^{3+} + 3e^- \rightarrow Au \quad (7)$$

$$2H^+ + 2e^- \rightarrow H_2 \quad (8)$$

Even in the field of electroless nickel plating, the reaction mechanism of hypophosphite has not yet reached a consensus. For electroless gold plating system, the reaction process of hypophosphite still needs to be verified by subsequent researchers.

Of course, the replacement reaction between Au(III)–DMH complex and Ni is also inevitable, which causes corrosion for Ni–P layer. However, because the reduction reaction replaces the partial replacement reaction, the degree of corrosion for Ni–P layer has been greatly reduced, thus improving the corrosion resistance of the coating. Also combined with element distribution of the coating based on XPS depth profiles, we deduce that the reduced gold atom preferentially deposited on "saddles" spaces between the two "mountains" on the Ni–P layer, as shown in the schematic diagram of Fig. 8(b) and S4† (ESI). The main products of the reduction reaction and the displacement reaction, including HPO_3^{2-} (or $H_2PO_3^-$) and Ni^{2+},

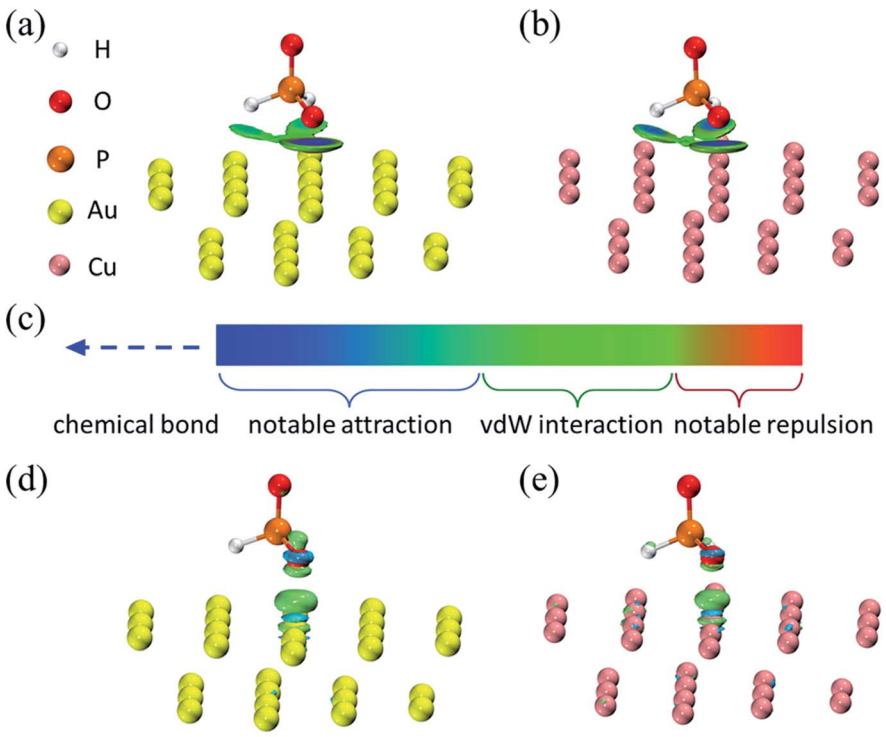

Fig. 14 Visual analyses for adsorption structures of hypophosphite on Au_{31} and Cu_{31} clusters: (a and b) IGMH analyses, (c) color bar for IGMH analysis, and (d and e) difference map of electron density.

Open Access Article. Published on 08 December 2021. Downloaded on 2/7/2026 7:15:34 PM.
This article is licensed under a Creative Commons Attribution-NonCommercial 3.0 Unported Licence.

have a higher concentration on the Ni–P surface than in the bulk of the bath, so they also spontaneously diffuse into the bulk of the bath. Whereas H_2 floats to the surface of the bath due to buoyancy.

3.5 Quantum chemical calculation

The deposition reaction taking place preferentially on the metal surface is closely related to the catalytic properties of the surface. Profiting from the catalysis by Ni, $H_2PO_2^-$ can play a reducing effect in the gold deposition process in this paper. This relationship between $H_2PO_2^-$ and Ni has been fully proven and studied in the field of nickel plating.[30,71,72] In the gold deposition process, nickel is a kind of substrate, so the deposition process has the characteristics of substrate catalytic reduction.[35] We are more concerned about whether there is autocatalytic reduction in addition to substrate catalysis, which can deepen our understanding of the reaction process.

In order to further understand the catalytic difference of gold for the reduction of $H_2PO_2^-$ compared with nickel at the molecular level, quantum chemical calculations were carried out. It is well known that Cu cannot catalyze the oxidation of $H_2PO_2^-$,[73] so the interaction between Cu and $H_2PO_2^-$ was also analyzed as a comparison to help further understand the interaction between Au and $H_2PO_2^-$. The structures of metal clusters are shown in Fig. S9† (ESI). The structures of $H_2PO_2^-$ adsorbed on Au_{31} and Cu_{31} clusters and the structural parameters of $H_2PO_2^-$ are shown in Fig. S10† (ESI) and Table S4† (ESI), respectively. $H_2PO_2^-$ adsorbed on the clusters through O atom, and its structures on Au_{31} and Cu_{31} clusters were similar according to Fig. S10 (ESI) and Table S4† (ESI), meaning that the catalytic properties of Au for $H_2PO_2^-$ may resemble that of Cu. Onabuta *et al.*[72] also reported that $H_2PO_2^-$ adsorbed on the copper surface *via* O atom by the first-principle study. Kunimoto *et al.*[74] reported that $H_2PO_2^-$ adsorbed on Ni clusters relying on H atoms, while O atoms were far away. The significantly different structures of $H_2PO_2^-$–Au and $H_2PO_2^-$–Ni indicate that Au is destined to have different catalytic properties for $H_2PO_2^-$ from Ni.

Through visual analysis methods, including Independent Gradient Model analysis based on Hirshfeld partition of molecular density (IGMH, 0.01 a. u.)[75,76] and difference map of electron density (0.006 a. u.), the interaction between $H_2PO_2^-$ and Au, as well as Cu, can be visually displayed, as shown in Fig. 14. The interaction type can be determined by comparing the color of the color bar (Fig. 14(c)) with the color-filled isosurface. It can be seen that there was a very broad and flat isosurface sandwiched between the $H_2PO_2^-$ and metal surface, which clearly portrayed the major interaction region. The isosurfaces in Fig. 14(a and b) were similar. They looked like three green circular pies, corresponding to the van der Waals action. A blue area appeared in the center of the pie between O and Au atoms, indicating a slightly stronger attraction than the van der Waals action, but the intensity had not yet reached the strength of chemical bonds, as the isosurface was not only composed of pure blue. Therefore, $H_2PO_2^-$ adsorbed on the Au and Cu surfaces in the weak interaction. Furthermore, since the blue around the center of the isosurface corresponding to the O–Au interaction was lighter than that corresponding to the O–Cu interaction, it is expected that the $H_2PO_2^-$–Au_{31} cluster interaction was weaker. The electron density difference map intuitively showed the change of the electron density after $H_2PO_2^-$ adsorbed on the metal surface, as shown in Fig. 14(d and e). The increase and decrease of electron density were represented by grass-green and sky-blue isosurfaces respectively, which also meant the strengthening and weakening of bonds respectively. It can be seen from Fig. 14(d and e) that the isosurface between O and Au atoms as well as Cu atoms were all grass-green, meaning that the electron density was reduced, which was not conducive to formate a chemical bond. IGMH analysis and electron density difference analysis revealed the nature of the interaction between $H_2PO_2^-$ and Au as well as Cu surfaces, that is, they relied on weak interaction to adsorb instead of chemical bonds. However, the stable adsorption of $H_2PO_2^-$ on the metal relying on the orbital interaction is the key to the high catalytic activity of the metal for $H_2PO_2^-$.[71,72] Quantum chemistry calculation results showed that the adsorption structures of $H_2PO_2^-$ on Au and Cu did not meet this requirement, meaning that there was no autocatalytic reduction in deposition process.

4. Conclusion

In this work, a green, stable, and environmentally friendly cyanide-free gold plating bath is developed with adding hypophosphite as a reducing agent into the Au(III)–DMH based plating bath. With the employ of NaH_2PO_2, the Au layer became denser, and the black pad phenomenon of the Ni–P layer was almost eliminated. However, the addition of NaH_2PO_2 did not change the crystal structure of the Au layer, and the preferred orientation was (111). XPS showed that P element was not introduced, so the Au layer was pure gold. XPS depth profiles suggested that there was a transition layer between the Au layer and the Ni–P layer, and the two layers were combined in an inlaid structure. This combination way allowed the coating to be firmly integrated even after 16 days of extreme temperature damage. When the concentration of NaH_2PO_2 is 10 g L^{-1}, the appearance of the Au layer was still yellow after neutral salt spray corrosion for 48 hours. The PDP and EIS tests showed that the E_{corr} was −0.191 V, the i_{corr} was 11.5 μA cm^{-2}, the porosity was 0.84%, and the R_{ct} was 11.31 kΩ cm^{-2} at this concentration. Compared with the coating deposited without NaH_2PO_2, the corrosion resistance was significantly improved. The plating baths in this work had good stability and were still clear after 210 days. Atomic absorption spectrum showed that the addition of NaH_2PO_2 made part of the replacement reaction replaced by the reduction reaction. Profit from this, the structure and corrosion resistance of the coatings were better. Quantum chemistry calculations showed that hypophosphite adsorbed on Au surface in a weak interaction manner, and Au was inactive for the catalysis of hypophosphite. In general, this study has successfully demonstrated the great potential of new paths for the realization of cyanide-free electroless gold plating.

 © 2021 The Author(s). Published by the Royal Society of Chemistry

Open Access Article. Published on 08 December 2021. Downloaded on 2/7/2026 7:15:34 PM.
This article is licensed under a Creative Commons Attribution-NonCommercial 3.0 Unported Licence.

Conflicts of interest

There are no conflicts to declare.

Acknowledgements

We greatly acknowledge the financial support from the National Natural Science Foundation of China (Grant No. 22178071). We also thank GHTECH (China) for providing commercial plating baths.

References

1 S. Dimitrijević, M. Rajčić-Vujasinović and V. Trujić, *Int. J. Electrochem. Sci.*, 2013, **8**, 6620–6646.
2 A. Bahramian, M. Eyraud, F. Vacandio and P. Knauth, *Microelectron. Eng.*, 2019, **206**, 25–44.
3 S. Ming, M. Pecht and M. A. E. Natishan, *Microelectron. J.*, 1999, **30**, 217–222.
4 A. Bahramian, M. Eyraud, S. Maria, F. Vacandio, T. Djenizian and P. Knauth, *Corros. Sci.*, 2019, **149**, 75–86.
5 V. K. Murugan, Z. G. Jia, G. J. Syaranamual, C. L. Gan, Y. Z. Huang and Z. Chen, *Microelectron. Reliab.*, 2016, **60**, 84–92.
6 T. Osaka, T. Misato, J. Sato, H. Akiya, T. Homma, M. Kato, Y. Okinaka and O. Yoshioka, *J. Electrochem. Soc.*, 2000, **147**, 1059.
7 Y. Okinaka, *Gold Bull.*, 2000, **33**, 117–127.
8 M. Kato, J. Sato, H. Otani, T. Homma, Y. Okinaka, T. Osaka and O. Yoshioka, *J. Electrochem. Soc.*, 2002, **149**, C164.
9 H. Honma and Y. Kagaya, *J. Electrochem. Soc.*, 1993, **140**, L135.
10 H. Honma and K. Hagiwara, *J. Electrochem. Soc.*, 1995, **142**, 81.
11 Y. Okinaka and M. Hoshino, *Gold Bull.*, 1998, **31**, 3–13.
12 T. Osaka, M. Kato, J. Sato, K. Yoshizawa, T. Homma, Y. Okinaka and O. Yoshioka, *J. Electrochem. Soc.*, 2001, **148**, C659.
13 T. Osaka, A. Kodera, T. Misato, T. Homma, Y. Okinaka and O. Yoshioka, *J. Electrochem. Soc.*, 1997, **144**, 3462.
14 T. A. Green and S. Roy, *J. Electrochem. Soc.*, 2006, **153**, C157.
15 B. Li, N. Li, G. Luo and D. Tian, *Surf. Coat. Technol.*, 2016, **302**, 202–207.
16 E. F. De Monlevade and W. Peng, *J. Electron. Mater.*, 2007, **36**, 783–797.
17 M. Schlesinger and M. Paunovic, *Modern electroplating*, John Wiley & Sons, 2011.
18 B. Wu, J. M. Huang, Z. M. Lv, Z. Y. Cui, G. H. Hu, J. Y. Luo, M. S. Selim and Z. F. Hao, *RSC Adv.*, 2020, **10**, 9768–9776.
19 L. Jin, J. Q. Yang, F. Z. Yang, D. P. Zhan, D. Y. Wu and Z. Q. Tian, *ACS Sustainable Chem. Eng.*, 2020, **8**, 14274–14279.
20 G. Lewis and C. F. Shaw III, *Inorg. Chem.*, 1986, **25**, 58–62.
21 G. Luo, G. H. Yuan and N. Li, *RSC Adv.*, 2016, **6**, 61341–61345.
22 X. F. Ren and M. Z. An, *RSC Adv.*, 2018, **8**, 2667–2677.
23 X. Q. Tu, Y. H. Zhang, D. Wang, M. Z. An, A. M. Liu, J. Q. Zhang and P. X. Yang, *J. Electrochem. Soc.*, 2020, **167**, 22506.
24 F. F. Huang and M. L. Huang, *J. Electrochem. Soc.*, 2018, **165**, D152.
25 L. Jin, C. Liu, F. Z. Yang, D. Y. Wu and Z. Q. Tian, *Electrochim. Acta*, 2019, **304**, 168–174.
26 J. S. Chen, Y. M. Fang, Q. Y. Qiu, L. X. You, J. Song, G. M. Zhang, G. N. Chen and J. J. Sun, *Green Chem.*, 2011, **13**, 2339–2343.
27 L. Jin, J. Q. Yang, F. Z. Yang, D. Y. Wu and Z. Q. Tian, *J. Electrochem. Soc.*, 2020, **167**, 22511.
28 K. Oyaizu, Y. Ohtani, A. Shiozawa, K. Sugawara, T. Saito and M. Yuasa, *Inorg. Chem.*, 2005, **44**, 6915–6917.
29 X. W. Yang, M. Z. An, Y. W. Zhang and L. Zhang, *Electrochim. Acta*, 2011, **58**, 516–522.
30 K. H. Krishnan, S. John, K. N. Srinivasan, J. Praveen, M. Ganesan and P. M. Kavimani, *Metall. Mater. Trans. A*, 2006, **37**, 1917–1926.
31 G. Milad, *Circuit World*, 2010.
32 Y. R. Wang, X. Y. Cao, W. C. Wang, N. Mitsuzak and Z. D. Chen, *Surf. Coat. Technol.*, 2015, **265**, 62–67.
33 N. Shaigan, S. N. Ashrafizadeh, M. Bafghi and S. Rastegari, *J. Electrochem. Soc.*, 2005, **152**, C173.
34 C. D. Iacovangelo, *J. Electrochem. Soc.*, 1991, **138**, 976.
35 C. D. Iacovangelo and K. P. Zarnoch, *J. Electrochem. Soc.*, 1991, **138**, 983.
36 W. J. Yao, D. X. Wu, Z. L. Xiao, Y. W. Wang and R. H. Yang, *Int. J. Electrochem. Sci.*, 2019, **14**, 9633–9646.
37 L. Bonin, V. Vitry and F. Delaunois, *Surf. Coat. Technol.*, 2020, **401**, 126276.
38 J. Creus, H. Mazille and H. Idrissi, *Surf. Coat. Technol.*, 2000, **130**, 224–232.
39 F. Neese, *Wiley Interdiscip. Rev.: Comput. Mol. Sci.*, 2012, **2**, 73–78.
40 F. Neese, *Wiley Interdiscip. Rev.: Comput. Mol. Sci.*, 2018, **8**, e1327.
41 A. V. Marenich, C. J. Cramer and D. G. Truhlar, *J. Phys. Chem. B*, 2009, **113**, 6378–6396.
42 D. Andrae, U. Haeussermann, M. Dolg, H. Stoll and H. Preuss, *Theor. Chim. Acta*, 1990, **77**, 123–141.
43 F. Weigend and R. Ahlrichs, *Phys. Chem. Chem. Phys.*, 2005, **7**, 3297–3305.
44 C. Adamo and V. Barone, *J. Chem. Phys.*, 1999, **110**, 6158–6170.
45 S. Grimme, S. Ehrlich and L. Goerigk, *J. Comput. Chem.*, 2011, **32**, 1456–1465.
46 T. Lu and F. W. Chen, *J. Comput. Chem.*, 2012, **33**, 580–592.
47 W. Humphrey, A. Dalke and K. Schulten, *J. Mol. Graph.*, 1996, **14**, 33–38.
48 Y. R. Wang, X. Y. Cao, Z. M. Wang, Z. D. Chen and N. Mitsuzaki, *Int. J. Electrochem. Sci.*, 2019, **14**, 8185–8194.
49 K. Xiao, Z. H. Bai, L. D. Yan, P. Yi, C. F. Dong, J. S. Wu, Y. T. Hu, R. L. Xiong and X. G. Li, *J. Mater. Sci.: Mater. Electron.*, 2018, **29**, 8877–8885.
50 Y. S. Won, S. S. Park, J. Lee, J. Y. Kim and S. J. Lee, *Appl. Surf. Sci.*, 2010, **257**, 56–61.

Open Access Article. Published on 08 December 2021. Downloaded on 2/7/2026 7:15:34 PM.
This article is licensed under a Creative Commons Attribution-NonCommercial 3.0 Unported Licence.

51 J. D. Lin and C. T. Chou, *Surf. Coat. Technol.*, 2019, **368**, 126–137.
52 A. J. Gould, P. J. Boden and S. J. Harris, *Surf. Technol.*, 1981, **12**, 93–102.
53 A. Lelevic and F. C. Walsh, *Surf. Coat. Technol.*, 2019, **369**, 198–220.
54 K. H. Kim, J. Yu and J. H. Kim, *Scr. Mater.*, 2010, **63**, 508–511.
55 Y. Wang, H. P. Liu, S. F. Bi, M. X. He, C. Y. Wang and L. X. Cao, *RSC Adv.*, 2016, **6**, 9656–9662.
56 D. G. Liu, H. Tian, L. J. Lin and W. C. Shi, *Surf. Eng.*, 2019, **35**, 913–918.
57 J. K. Li, C. Sun, M. Roostaei, M. Mahmoudi, V. Fattahpour, H. B. Zeng and J. L. Luo, *Mater. Chem. Phys.*, 2021, **267**, 124618.
58 K. G. Keong, W. Sha and S. Malinov, *J. Alloys Compd.*, 2002, **334**, 192–199.
59 K. Abdi Alghanab, D. Seifzadeh, Z. Rajabalizadeh and A. Habibi Yangjeh, *Surf. Coat. Technol.*, 2020, **397**, 125979.
60 J. Z. Zhou, P. Liu, Z. Y. Liu, J. Zhang and X. Huang, *Chem. Eng. J.*, 2020, **381**, 122702.
61 G. Valiulienė, A. Žielienė and V. Jasulaitienė, *Trans. IMF*, 2006, **84**, 162–167.
62 N. V. Sotskaya and O. V. Dolgikh, *Russ. J. Electrochem.*, 2005, **41**, 1336–1340.
63 V. K. Murugan, Z. G. Jia, G. J. Syaranamual, Y. Z. Huang and Z. Chen, *J. Mater. Sci.*, 2017, **52**, 9834–9849.
64 X. B. Liu, H. Q. Liu, Y. F. Liu, X. M. He, C. F. Sun, M. D. Wang, H. B. Yang and L. H. Qi, *Composites, Part B*, 2013, **53**, 347–354.
65 S. S. Latthe, P. Sudhagar, A. Devadoss, A. M. Kumar, S. Liu, C. Terashima, K. Nakata and A. Fujishima, *J. Mater. Chem. A*, 2015, **3**, 14263–14271.
66 Y. Gong, J. W. Geng, J. Huang, Z. Chen, M. L. Wang, D. Chen and H. W. Wang, *Surf. Coat. Technol.*, 2021, **417**, 127208.
67 Y. X. Zhu, J. J. Jiang, L. J. Yang, C. Xu, Q. K. Zhang, X. L. Zhu, X. Li, J. Jin, Q. Zhou and Z. L. Song, *Surf. Coat. Technol.*, 2021, 127415.
68 M. A. Ehsan, A. M. Kumar, R. K. Suleiman and A. S. Hakeem, *Surf. Coat. Technol.*, 2021, **418**, 127253.
69 X. J. Wang and Y. Cao, *J. Ind. Eng. Chem.*, 2020, **82**, 324–332.
70 T. N. Vorobyova, S. K. Poznyak, A. A. Rimskaya and O. N. Vrublevskaya, *Surf. Coat. Technol.*, 2004, **176**, 327–336.
71 M. Kunimoto, T. Shimada, S. Odagiri, H. Nakai and T. Homma, *J. Electrochem. Soc.*, 2011, **158**, D585.
72 Y. Onabuta, M. Kunimoto, H. Nakai and T. Homma, *Electrochim. Acta*, 2019, **307**, 536–542.
73 S. Ghosh, *Thin Solid Films*, 2019, **669**, 641–658.
74 M. Kunimoto, K. Endo, H. Nakai and T. Homma, *Electrochim. Acta*, 2013, **100**, 311–316.
75 C. Lefebvre, G. Rubez, H. Khartabil, J. C. Boisson, J. Contreras García and E. Hénon, *Phys. Chem. Chem. Phys.*, 2017, **19**, 17928–17936.
76 T. Lu and Q. X. Chen, Independent gradient model based on Hirshfeld partition (IGMH): A new method for visual study of interactions in chemical systems, 2021, https://chemrxiv.org/engage/chemrxiv/article-details/619e3e807c89166dba431bd0.

 © 2021 The Author(s). Published by the Royal Society of Chemistry